Applied Soft Computing Journal 203 (2026) 116305

Contents lists available at ScienceDirect

Applied Soft Computing

journal homepage: www.elsevier.com/locate/asoc

ConvLSTM-based modeling of magnetic domain evolution in electric motor core materials

Hao Zhang [a], Qingxin Yang [a,b], Yifan Chen [a], Yongjian Li [a], Changgeng Zhang [a,*]

[a] State Key Laboratory of Intelligent Power Distribution Equipment and System, Hebei University of Technology, Tianjin, 300130, China
[b] School of Electrical and Electronic Engineering, Tianjin University of Technology, Tianjin, 300384, China

HIGHLIGHTS

- A ConvLSTM-based prediction model for the dynamic evolution of magnetic domains in non-oriented silicon steel is established.
- A novel magnetic domain image data processing method was proposed, and image features were extracted for model training.
- The validity and applicability of the proposed model were verified through the use of similarity metrics.

ARTICLE INFO

Keywords:
Magnetic Domain
Machine Learning
Magnetization process
Microstructure

ABSTRACT

Traditional modeling of energy loss in magnetic materials for electric machines primarily relies on empirical models based on macroscopic magnetic parameters. However, when subjected to transient excitations from modern control strategies, these models often fail to capture the dynamic magnetic response, since these models do not sufficiently represent the intrinsic, microstructure-dependent magnetization processes. The spatiotemporal evolution of magnetic domains serves as a crucial bridge linking microscopic magnetic mechanisms to macroscopic energy loss, playing a key role in understanding internal energy dissipation processes. In response to this challenge, this work presents a ConvLSTM-based predictive framework that combines convolutional feature extraction with temporal sequence modeling to predict the evolution of intrinsic magnetization states from historical magnetic domain patterns. The results show that the framework can predict magnetic domain motion patterns and magnetization processes under complex spatiotemporal conditions, and that incorporating magnetic domain boundary and grayscale texture features improves the prediction accuracy by up to 13.01%. This approach provides a robust tool for analyzing magnetic microstructures, offering valuable insights for optimizing magnetic material properties and enhancing the performance of electric motors.

1. Introduction

In recent years, the rapid growth of global energy consumption and the increasing demand for energy-efficient systems have posed significant challenges to the optimization of energy conversion devices, particularly electric motors. As key components in various industrial applications, electric motors are prone to energy losses during operation, with losses in magnetic materials accounting for a substantial portion. Therefore, accurate modeling and prediction of magnetic material losses are crucial for enhancing motor efficiency and reducing energy consumption [1–4].

The dynamic evolution of microscopic magnetic domains fundamentally determines the macroscopic loss behavior of magnetic materials. Under the influence of magnetic fields, complex domain evolution governs the magnetization process and energy dissipation characteristics. Therefore, accurately characterizing and predicting domain dynamics is vital to understanding the loss mechanisms in magnetic materials and developing low-loss, high-performance motor components [5–8].

Traditional loss-characterization methods rely heavily on macroscopic hysteresis and loss measurements and semi-empirical formulations constrained by a small set of global quantities. Although these methods can partially predict material loss behavior, they often fail to reveal the underlying microscopic mechanisms, particularly the influence of domain structure evolution on magnetization. Additionally, these experimental techniques are time-consuming, costly, and complex,

* Corresponding author.
E-mail address: changgeng.zhang@hebut.edu.cn (C. Zhang).

https://doi.org/10.1016/j.asoc.2026.116305
Received 8 August 2025; Received in revised form 24 February 2026; Accepted 24 August 2026
Available online 25 August 2026
1568-4946/© 2026 Elsevier B.V. All rights are reserved, including those for text and data mining, AI training, and similar technologies.

presenting challenges in sample preparation and data processing.

With the rapid advancement of artificial intelligence, machine learning (ML) techniques have emerged as promising tools for materials science research [9–11]. In particular, convolutional neural networks (CNNs) have demonstrated strong performance in processing magnetic domain images by capturing spatial correlations and structural features [12–17]. By leveraging ML, it becomes possible to establish data-driven links between microscopic domain characteristics and macroscopic magnetic responses, offering an alternative route for modeling complex magnetic behaviors. Nevertheless, the intrinsic complexity of ferromagnetic materials—such as the multiple local energy minima (LEM) states induced by hysteresis—poses challenges for conventional modeling, and purely spatial models may be insufficient to capture the history-dependent nature of domain evolution.

To enable efficient analysis of the spatiotemporal evolution of magnetic domains, this study develops a ConvLSTM-based predictive framework that leverages convolutional feature extraction and temporal sequence modeling to capture domain dynamics [18–21]. In addition, to enhance the quality of magnetic domain imagery, a Large-Mask image inpainting (LaMa) model is employed to reconstruct and refine Magneto-optical Kerr effect (MOKE) images by suppressing artifacts and defects, thereby ensuring a high-fidelity dataset for model training and evaluation. Furthermore, the domain boundary information and the grayscale texture cues are explicitly integrated as feature enhancements to augment the representation of physically relevant structures within the domain patterns. The resulting framework enables accurate prediction of magnetic domain evolution, establishing a robust methodology for microstructure-informed analysis of magnetic materials and motor-core performance.

2. Experimental

The experimental sample used in this study was non-oriented electrical steel sheet B35A270. The sample sheet was sectioned into square specimens measuring 10 mm × 10 mm using wire electrical discharge machining. Subsequently, the spmple surface was prepared using standard metallographic procedures comprising mounting, grinding, and final polishing to achieve a mirror-like finish satisfying the optical requirements of Kerr microscopy prior to imaging.

Magnetic domain evolution was observed using a NEOARK Magneto-optical Kerr effect microscope system, as illustrated in Fig. 1(a). In MOKE microscopy, a linearly polarized light beam is reflected from the ferromagnetic surface, where the polarization undergoes Kerr rotation proportional to the local magnetization component along the sensitivity axis. This rotation is subsequently converted into optical intensity contrast within the recorded images, enabling spatially resolved visualization of magnetic domain structures [22–25].

During a complete hysteresis-loop scan, the applied magnetic field was linearly ramped from + 500 Oe to −500 Oe and then back to + 500 Oe. Magnetic domain images were acquired continuously at a constant scanning rate, yielding a total of 1260 consecutive frames. A calibrated temporal synchronization procedure was used to establish a one-to-one correspondence between the image index and the applied field, thereby producing a spatiotemporally correlated, time-resolved MOKE sequence of domain evolution, as shown in Fig. 1(b). These 1260 images constitute a single temporally ordered sequence spanning one complete hysteresis loop rather than a collection of independent static snapshots. The dataset used for model training is constructed from this sequence using a sliding window strategy. Detailed information regarding this process is provided in Section 3.4.

3. Machine learning for microstructure analysis

3.1. Data preprocessing

To enhance the MOKE image dataset, we apply the LaMa inpainting model to repair corrupted regions, thereby ensuring high-fidelity inputs for model training [26]. Reliable inpainting requires a precise defect mask for each individual frame. In our experiments, the divergent magneto-optical responses of defective and non-defective regions induce a field-dependent discrepancy in surface reflectance. Specifically, defect features are inconspicuous and difficult to characterize under high applied fields, whereas they become prominent in low-field regions. This dynamic behavior renders a single static mask insufficient for restoring the full image sequence across the complete field range [27]. To construct a field-dependent mask, Otsu thresholding is applied to each frame to obtain an adaptive binarization threshold [28,29]. The threshold–field curve exhibits a typical symmetric distribution with respect to the applied field, as shown in Fig. 2(a), and it correlates with the hysteresis characteristics of the material. Otsu's method determines a global gray-level threshold by maximizing the between-class variance between the foreground and background populations, and it is well suited for the MOKE images.

Based on the threshold–field curve and the corresponding domain patterns, the field range is partitioned into three distinct intervals. The first interval represents low fields near the demagnetized state. The second covers the coercive-field region, where both the threshold and the domain structure undergo rapid evolution. The third pertains to high fields approaching saturation, where defect contrast is minimal. Within these intervals, representative field values are selected as key reference points, as indicated in Fig. 2(a), and defect-mask templates are defined accordingly. For intermediate field values, the corresponding masks are generated via pixel-wise linear interpolation between the templates at the nearest key points. This procedure yields a smooth dynamic mask that varies continuously with the applied field.

A comparison between the original domain images in Fig. 2(c) and

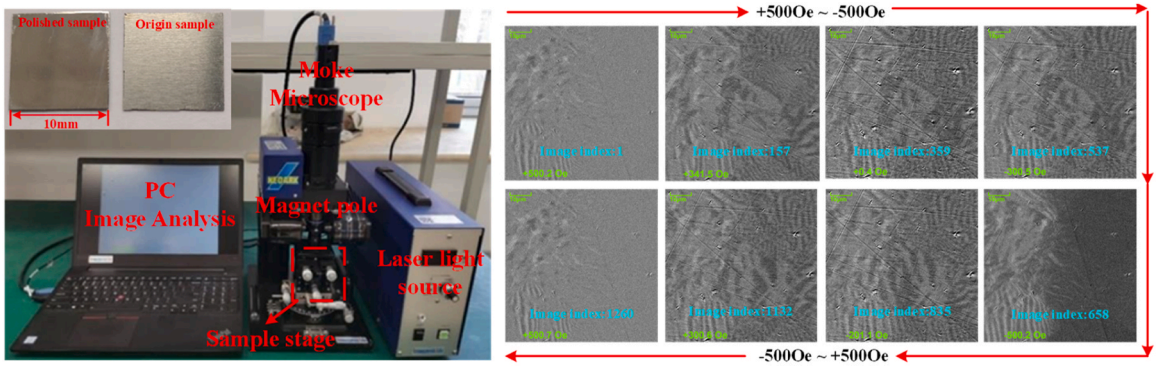


Fig. 1. (a) MOKE imaging setup and specimen. (b) MOKE domain image sequence acquired over a full hysteresis loop scan.

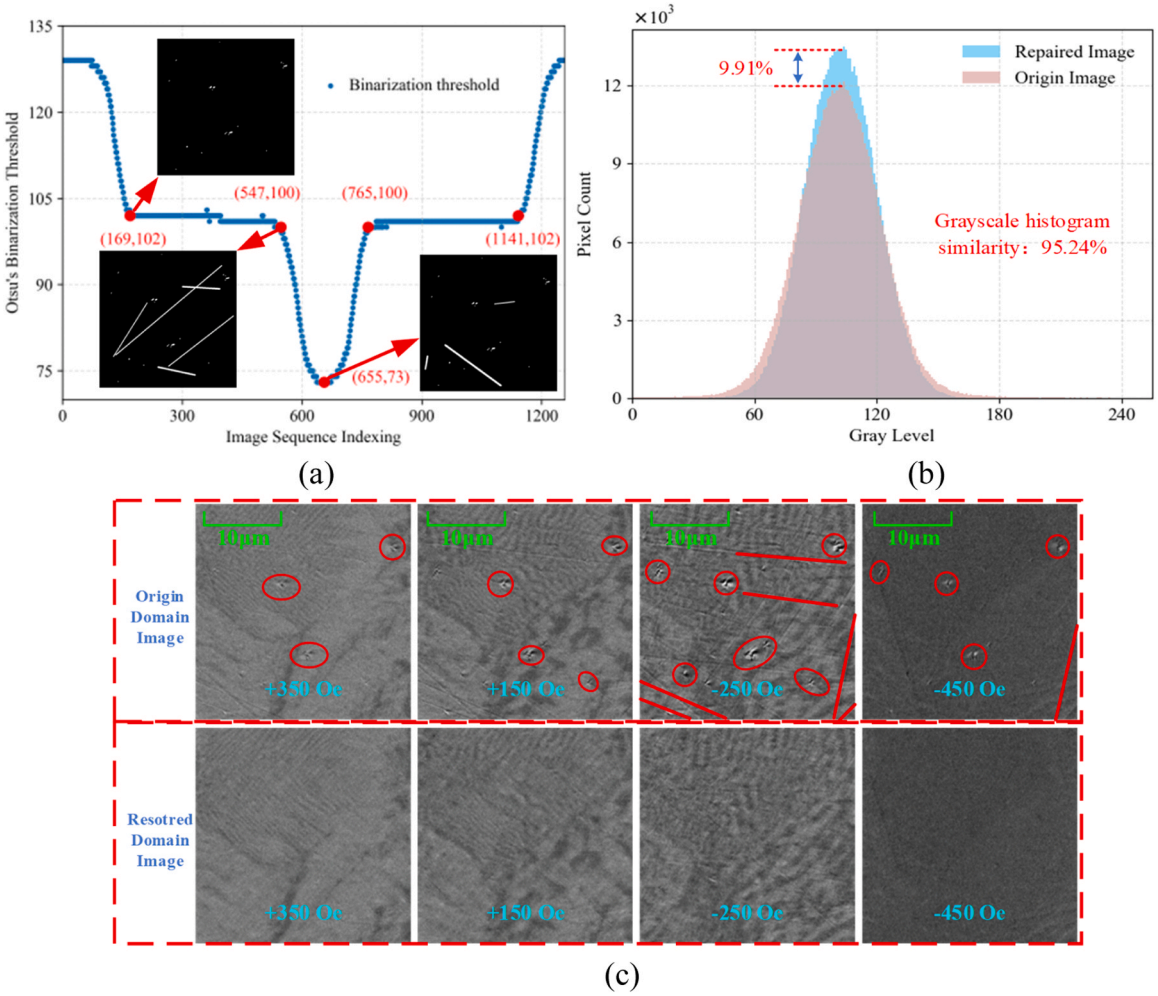


Fig. 2. Field-adaptive defect masking and LaMa inpainting for MOKE image restoration. (a) Otsu threshold and applied field. (b) Grayscale histogram similarity. (c) Comparison of original and restored MOKE domain images.

the LaMa restoration results indicates a 9.91% increase in the peak intensity of the grayscale histogram after restoration. This behavior suggests that artifact interference is effectively suppressed while the overall brightness is enhanced. The similarity between grayscale histograms before and after restoration is quantified by the histogram-intersection metric, as given by the following expression:

$$G(a,b) = \frac{\sum_{i=0}^{255}\min(a_i,b_i)}{\sum_{i=0}^{255}a_i} \times 100\% \tag{1}$$

where a_i and b_i denote the pixel counts at gray level i in the original and inpainted images, respectively. The $G(a,b)$ quantifies the similarity between the two gray-level histograms. As shown in Fig. 2(b), the histogram-intersection similarity reaches 95.24%, indicating that the processed dataset improves the signal-to-noise ratio in artifact regions while preserving the intrinsic distribution characteristics of pixel intensities. The resulting dataset provides a high-quality basis for subsequent construction of the neural network models.

3.2. Magnetic domain contour characteristics

Regarding the modeling of dynamic magnetic domain evolution in non-oriented silicon steel, standard convolutional operators often struggle to fully capture the texture variations induced by stochastic domain wall motion and local magnetic moment reversals. Physically, the geometry and evolution of domain walls play a central role in shaping the observed patterns. In classical domain theory, the density of exchange energy is proportional to the square of the gradient of magnetization. Therefore, the regions with steep gradients indicate the concentration of exchange energy and potential pinning sites.

In time-resolved MOKE imagery, sharp spatial transitions in intensity inherently correspond to these domain boundaries. Instead of treating these transitions merely as generic image edges, we interpret them as a representation of the domain wall network. Explicitly integrating this boundary information provides a physically meaningful constraint that supplements the representational capacity of the network. This approach not only aids in learning the spatiotemporal evolution mechanisms but also significantly improves the contour fidelity of the predicted results.

To operationalize this boundary constraint, we compute a Sobel gradient magnitude map $E(H_i)$ from each restored grayscale MOKE image to delineate regions with abrupt intensity transitions [30]. The Sobel operators are defined as:

$$G_x\left(x,y\right) = \begin{bmatrix} -1 & 0 & 1 \\ -2 & 0 & 2 \\ -1 & 0 & 1 \end{bmatrix} * I\left(x,y\right) \tag{2}$$

$$G_y\left(x,y\right) = \begin{bmatrix} -1 & -2 & -1 \\ 0 & 0 & 0 \\ 1 & 2 & 1 \end{bmatrix} * I\left(x,y\right) \tag{3}$$

where $I(x, y)$ denotes the pixel intensity of the restored grayscale image

and "∗" denotes 2D convolution. The final gradient magnitude is computed by the Euclidean norm.

$$|\nabla I(x,y)| = \sqrt{G_x^2(x,y) + G_y^2(x,y)} \tag{4}$$

The derived gradient magnitude map delineates the domain wall network and serves as the boundary feature channel in the physics-guided input representation. Fig. 3 illustrates a representative example of Sobel-based boundary extraction applied to magnetic domain images.

3.3. Gray-level co-occurrence matrix

During the varying magnetic field process, the grayscale evolution of MOKE images differs markedly across the hysteresis loop. When the applied field approaches the coercive field, domain nucleation and rapid domain wall motion lead to pronounced changes in contrast. However, following this phase of rapid domain wall displacement, the domain pattern tends to evolve more gradually. This subsequent evolution is often manifested as subtle, orientation-dependent texture variations and local intensity correlations. The information of local rotation of magnetic moments encoded by fine-grained grayscale cues can be lost in binary magnetic domain maps $B(H_i)$. However, using raw grayscale cues as input faces severe challenges due to inconsistent reflection coefficients, which degrade the signal-to-noise ratio of domain images.

Relying on raw intensity would require the network to implicitly learn to suppress these low-frequency optical noise signals. To address this while adhering to the underlying physics, we instead represent grayscale information using texture descriptors derived from the Gray-Level Co-occurrence Matrix (GLCM). These descriptors emphasize local gray-level correlations and directional texture statistics, which act as statistical proxies for the directionality and texture anisotropy of the domain patterns. Crucially, they exhibit reduced sensitivity to global brightness shifts [31], providing robust complementary cues to the magnetization and boundary representations.

By quantifying the normalized joint probability distribution $P(i, j)$ of gray-level (i, j) separated by a displacement vector denoted by distance d and angle θ, GLCM-based descriptors can capture anisotropic texture characteristics of magnetic domain structures. We compute three commonly used GLCM features, namely contrast (G_{ct}), homogeneity (G_{hg}) and energy (G_{en}):

$$G_{ct} = \sum_{i=0}^{N-1}\sum_{j=0}^{N-1}(i-j)^2 \cdot P(i,j) \tag{5}$$

$$G_{hg} = \sum_{i=0}^{N-1}\sum_{j=0}^{N-1}\frac{P(i,j)}{1+|i-j|} \tag{6}$$

$$G_{en} = \sum_{i=0}^{N-1}\sum_{j=0}^{N-1}P(i,j)^2 \tag{7}$$

where N denotes the number of gray levels, and $P(i, j)$ is the normalized co-occurrence probability of a pixel with gray level i and a pixel with gray level j.

Fig. 4 illustrates the directional GLCM-based texture maps computed at a fixed distance $d = 2$ for four angles(θ=0°,45°,90°,135°). The directional GLCM maps $G(H_i)$ extract the directional texture of grayscale cues while discarding absolute magnitude information, and are utilized as additional network inputs alongside the binary domain images $B(H_i)$.

3.4. Predictive model of magnetic domain structure

The dynamic evolution of magnetic domains is a prototypical spatiotemporal process under an applied excitation field. On the one hand, hysteresis and domain wall pinning introduce pronounced history dependence, so that accurate prediction requires incorporating history information [32]. On the other hand, domain patterns are inherently structured in space. Microstructural heterogeneity and inter-domain interactions give rise to strong local correlations, and domain changes tend to propagate through neighboring regions. These considerations motivate a modeling framework that can simultaneously preserve spatial topology and temporal memory. Accordingly, we employ a Convolutional Long Short-Term Memory (ConvLSTM) network. Mathematically, the ConvLSTM can be defined as:

$$\begin{cases} \mathbf{G}_i^{(t)} = \Phi\left(\mathbf{K}_{zi} * \mathbf{Z}^{(t)} + \mathbf{K}_{pi} * \mathbf{P}^{(t-1)} + \mathbf{K}_{si} \odot \mathbf{S}^{(t-1)} + \mathbf{b}_i\right) \\ \mathbf{G}_f^{(t)} = \Phi\left(\mathbf{K}_{zf} * \mathbf{Z}^{(t)} + \mathbf{K}_{pf} * \mathbf{P}^{(t-1)} + \mathbf{K}_{sf} \odot \mathbf{S}^{(t-1)} + \mathbf{b}_f\right) \\ \mathbf{S}^{(t)} = \mathbf{G}_f^{(t)} \odot \mathbf{S}^{(t-1)} + \mathbf{G}_i^{(t)} \odot \Psi\left(\mathbf{K}_{zc} * \mathbf{Z}^{(t)} + \mathbf{K}_{pc} * \mathbf{P}^{(t-1)} + \mathbf{b}_c\right) \\ \mathbf{G}_o^{(t)} = \Phi\left(\mathbf{K}_{zo} * \mathbf{Z}^{(t)} + \mathbf{K}_{po} * \mathbf{P}^{(t-1)} + \mathbf{K}_{so} \odot \mathbf{S}^{(t)} + \mathbf{b}_o\right) \\ \mathbf{P}^{(t)} = \mathbf{G}_o^{(t)} \odot \Psi(\mathbf{S}^{(t)}) \end{cases} \tag{8}$$

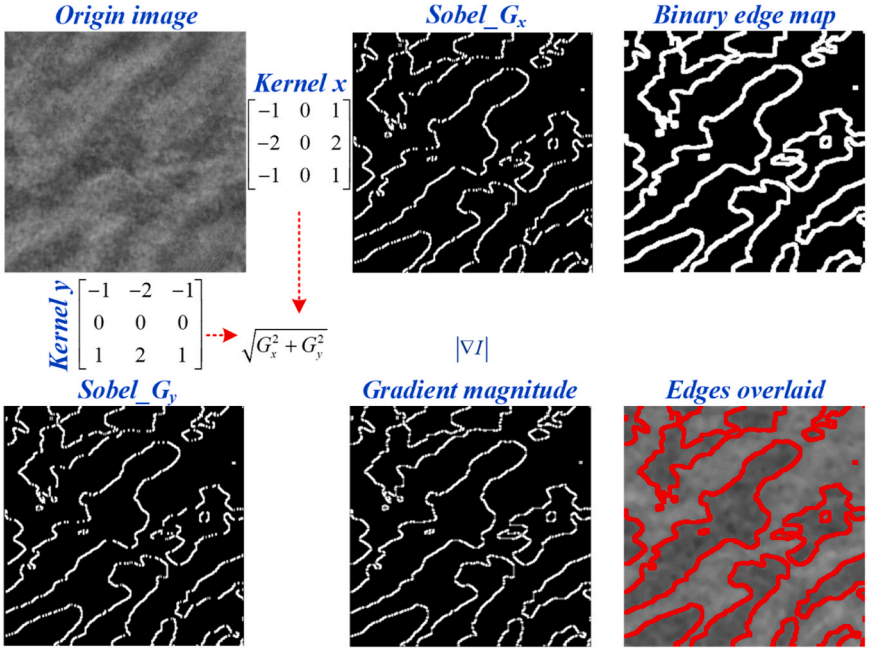


Fig. 3. Extraction of the domain wall network using the Sobel operator.

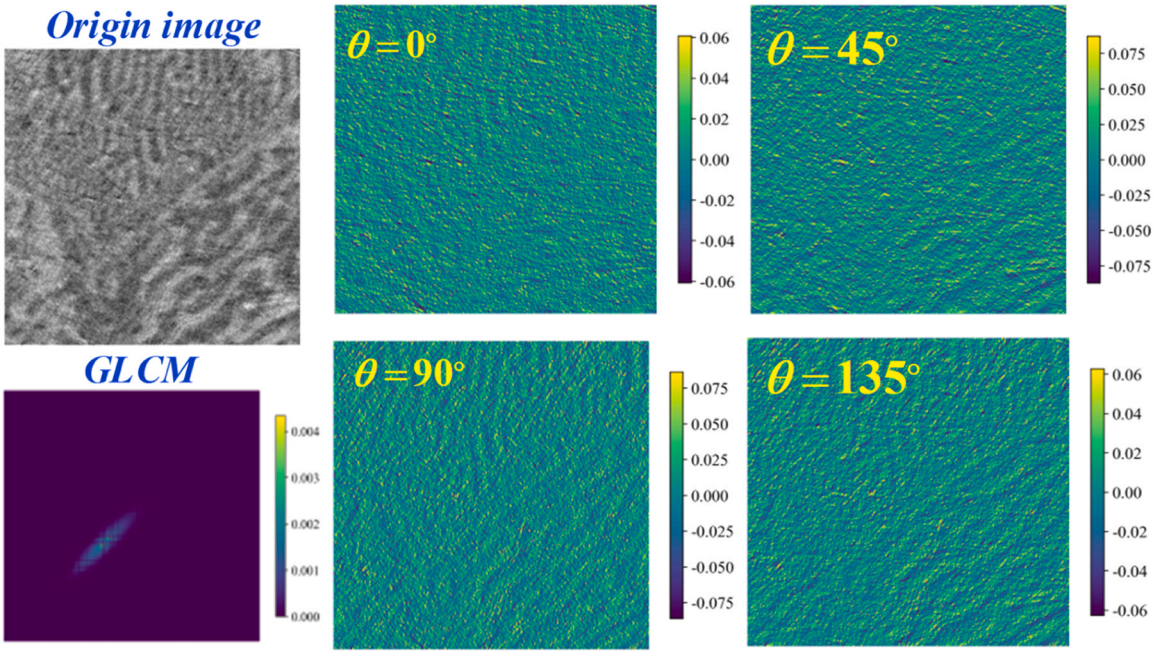


Fig. 4. Directional GLCM-based texture maps of magnetic domain images (θ=0°, 45°, 90°,135°, d = 2).

where $\boldsymbol{Z}^{(t)}$, $\boldsymbol{P}^{(t)}$, and $\boldsymbol{S}^{(t)}$ denote input tensor, hidden state, and cell state at time t, respectively; $\mathbf{G}_i^{(t)}$, $\mathbf{G}_f^{(t)}$, and $\mathbf{G}_o^{(t)}$ represent the input gate, forget gate, and output gate; $\boldsymbol{K}_{Z^*}$, $\boldsymbol{K}_{P^*}$, $\boldsymbol{K}_{S^*}$ and $\boldsymbol{b}_*$ are the corresponding convolutional weight tensors and bias terms; $\Phi(\cdot)$ and $\Psi(\cdot)$ denote the sigmoid and hyperbolic tangent activation functions; * represents the 2D convolution operation, and $\odot$ denotes the element-wise product.

In our framework, the ConvLSTM uses a physics-guided multi-channel representation F_i derived from the MOKE sequence, where each channel serves as an observable proxy for a major energy contribution as shown in Fig. 5. The exchange energy E_{ex} mainly concentrates in the domain wall region because it is associated with spatial variations of magnetization. Therefore, we use the boundary feature map $E(H_i)$ to highlight domain wall locations and local wall-related changes. The Zeeman energy E_z is determined by the applied field and the domain magnetization state. Accordingly, the binary map $B(H_i)$ encodes the domain state, which together with the applied field H_i, provides a direct proxy for field-driven energy change. The magnetocrystalline anisotropy energy E_{an} depends on magnetization orientation relative to the easy axis, which is reflected in the domain pattern orientation and texture. Thus, we construct the texture map $G(H_i)$ to describe directional correlations and texture evolution as an anisotropy-related descriptor.

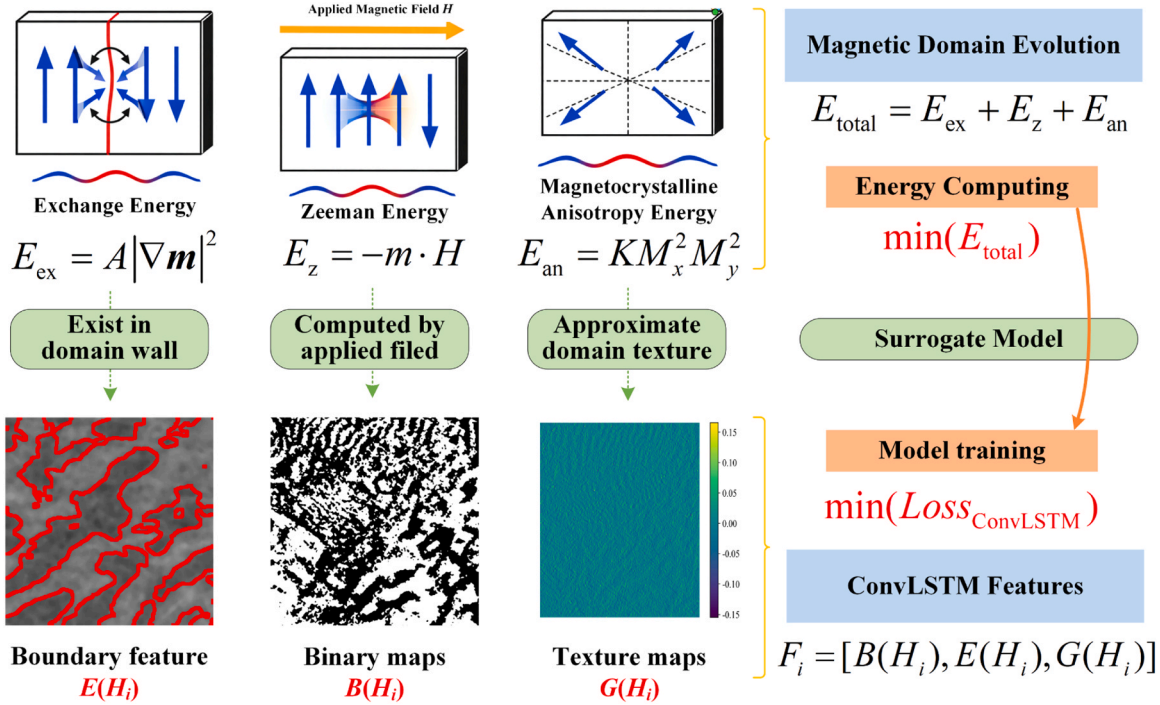


Fig. 5. Linking micromagnetic energy contributions to ConvLSTM input features.

The ConvLSTM is trained to learn the spatiotemporal mapping on these descriptors, rather than fitting arbitrary image intensities.

The input of the proposed model is defined as a four-dimensional spatio-temporal tensor, with its dimensions denoted as [T, H, W, F]. Here, T represents the length of the input historical sequence; H and W denote the height and width of the preprocessed images, respectively; and F represents the multiple feature channels. The network adopts an encoder–forecasting architecture, as shown in Fig. 6.

Both the encoding and forecasting networks are implemented by stacking multiple ConvLSTM layers. The detailed structural configuration, including the kernel sizes of each layer, is provided in Table 1.

For consistency of network input dimensions, all feature maps are resized to 256 × 256 pixels. The dataset consists of 1260 temporally ordered frames acquired continuously over one complete hysteresis loop. The samples are generated from this single time resolved sequence using a sliding window strategy. In particular, an input subsequence (F_{i-T+1}, …, F_i) with length T is used to predict the subsequent frames (F_{i+1}, …, F_{i+K}) over a prediction horizon K. Applying this sliding window to a sequence of length N yields N - (T + K) + 1 input–target pairs, enabling the model to learn from overlapping spatiotemporal contexts. To enhance model robustness and generalization capability, data augmentation is applied to the raw MOKE images prior to feature extraction. Three rotated images (45°, 90°, 135°) and one translated image are generated for each original frame. Feature channels are then recomputed for each augmented frame, ensuring that gradient-based maps and GLCM-based descriptors remain consistent with the transformed image axes. The dataset is partitioned into training, validation, and testing subsets with a split ratio of 8:1:1. The model is trained using the Adam optimizer with early stopping to mitigate overfitting. The experimental settings and training hyperparameters are summarized in Table 2.

The ConvLSTM is trained by minimizing a pixel-wise mean squared error between the predicted and ground truth binary domain images, averaged over all spatial locations and time steps in the prediction window. The training loss is defined as:

Table 1
The structural parameters of encoding and forecasting network.

Layers name	Input size	Output size	Kernel size	stride	padding
Input	256	128	4	2	1
ConvLSTM1	128	64	4	2	1
ConvLSTM2	64	64	3	1	1
ConvLSTM3	64	128	4	2	1
ConvLSTM4	128	256	4	2	1
Output	256	256	3	1	1

Table 2
Main training hyperparameters of the ConvLSTM model.

Parameter name	Value
Max epochs	200
Batch Size	16
Initial learning rate	1e-3
Learning-rate schedule	StepLR (step=100, γ=0.5)
Weight decay	1e-4
Early Stopping	patience 10 (val loss)
Optimizer	Adam
Loss function	MSELoss

$$\mathscr{L} = \frac{1}{K}\sum_{k=1}^{K}(\hat{y}_k - y_k)^2 \tag{9}$$

where y_k and $\hat{y}_k$ denote the ground truth and predicted pixel values, respectively. The index k enumerates all pixel values across the predicted frames and all spatial locations, and K is the total number of such pixel values.

4. Results and discussion

To evaluate the effectiveness of the proposed physics-guided representation, multiple ablation experiments were conducted using the

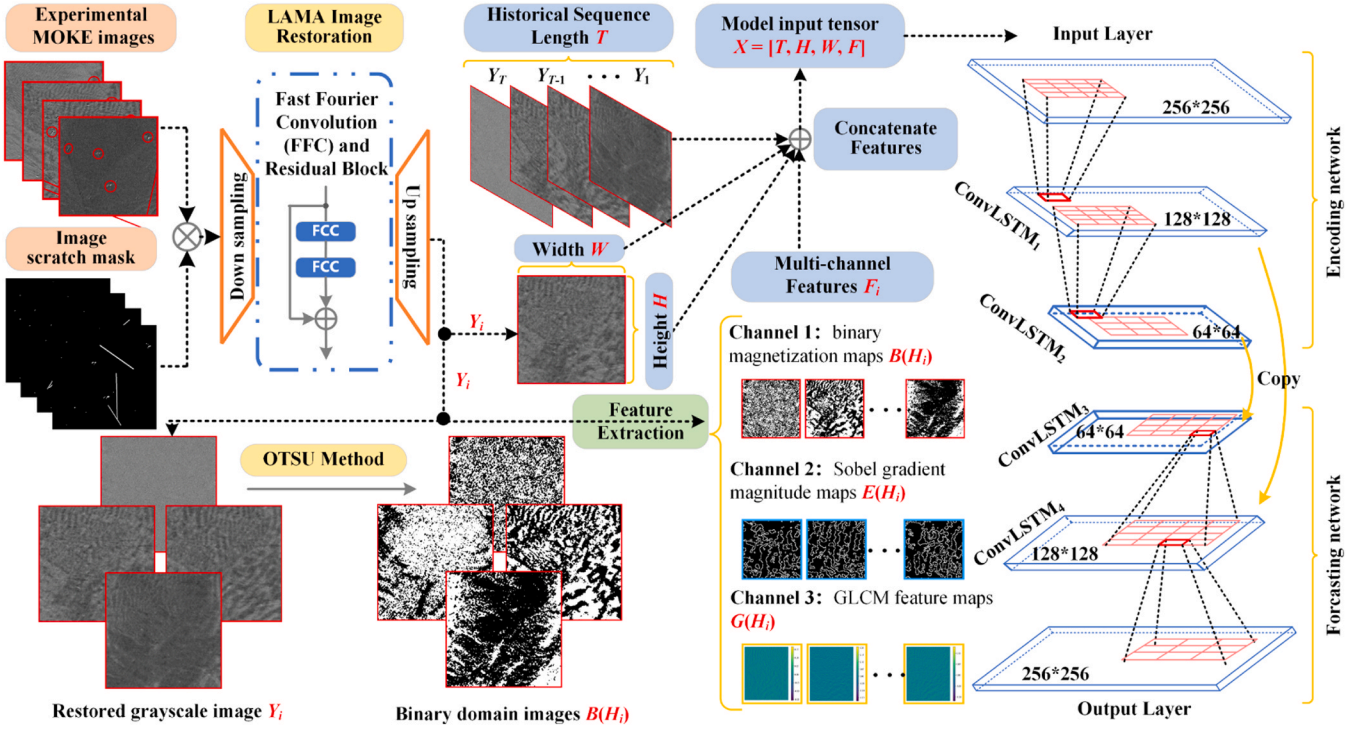


Fig. 6. Physically motivated feature channels input and ConvLSTM architecture.

ConvLSTM architecture with individual feature channels selectively removed. The model performance was assessed by examining the fidelity of domain wall motion and morphology, the preservation of grayscale intensity and texture evolution, and the consistency of macroscopic magnetic responses derived from the predicted domain patterns.

4.1. Ablation analysis of boundary feature

The model outputs are converted into a sequence of binary domain images using a fixed threshold to enable direct comparison with the binary ground truth images and facilitate quantitative evaluation. Fig. 7 compares the domain evolution predicted by the proposed model with an ablated variant where the Sobel based boundary channel is removed. Without explicit boundary information, the predictions tend to show blurred contours and isolated noise, and these artifacts become more severe as the prediction steps increase. In contrast, the proposed model better maintains the continuity of domain wall motion and generates sharper, more physically realistic boundaries in both the full field view and the zoomed region.

To quantify these observations, magnetic domain contours are tracked across the applied-field sequence, as illustrated in Fig. 8(a). For each field step H_i, the domain area $A(H_i)$ and contour perimeter $P(H_i)$ are extracted from the Moke image using the calibrated pixel size. Two morphology descriptors are then computed. The circularity is defined as:

$$C(H_i) = \frac{4\pi A(H_i)}{P(H_i)^2} \tag{10}$$

which decreases as the boundary becomes longer and more irregular relative to its enclosed area. In addition, fractal dimension is used to characterize boundary complexity [33]:

$$D(H_i) = \frac{\log P(H_i)}{\log \sqrt{A(H_i)}} \tag{11}$$

with this definition, a larger $D(H_i)$ indicates that the perimeter grows

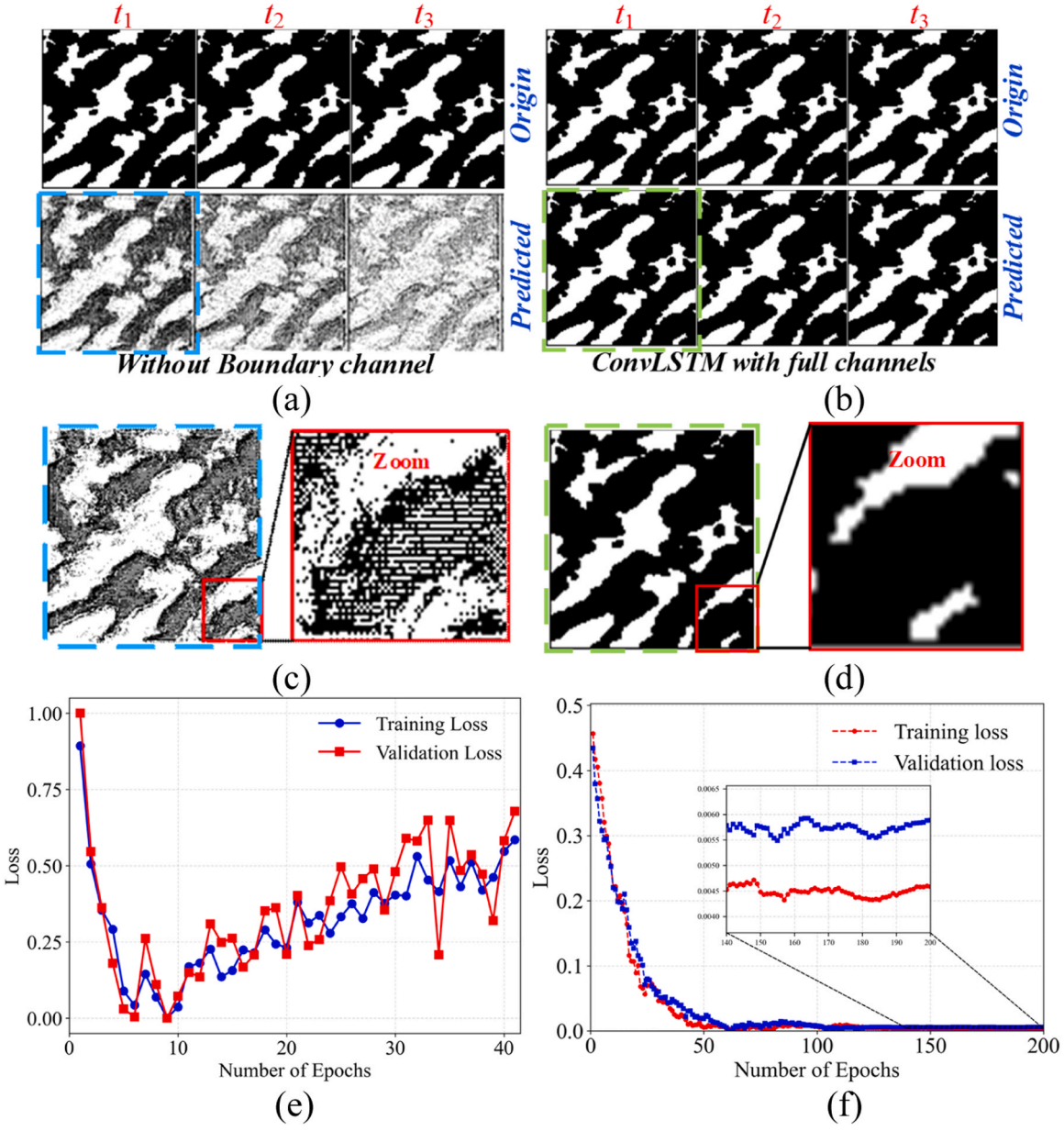


Fig. 7. ConvLSTM boundary-feature ablation versus full model. (a)-(b) ground-truth and predicted domain images. (c)-(d) zoomed comparison of a representative region. (e)-(f) training and validation loss curves.

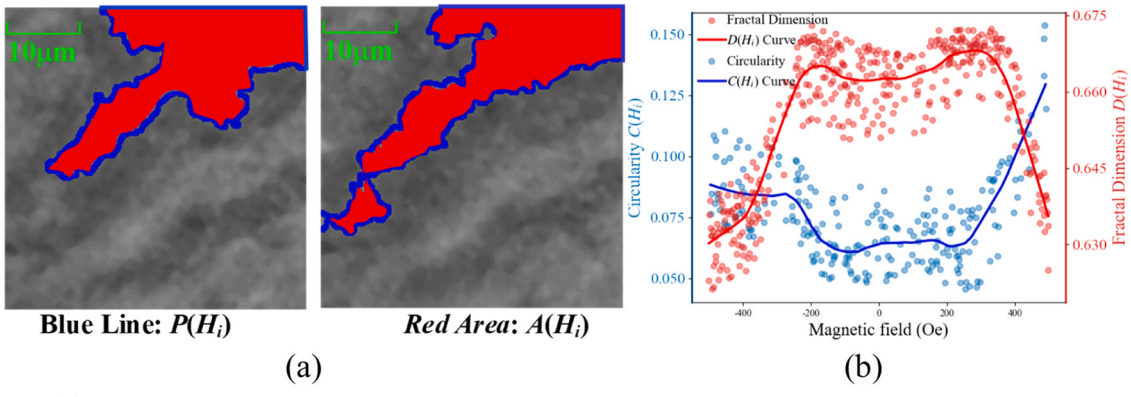


Fig. 8. (a) Magnetic domain evolution in response to time varying magnetic fields, (b) Morphology descriptors in the model-predicted circularity and fractal dimension of magnetic domains.

more rapidly relative to the area, which is consistent with a more tortuous and strongly roughened domain boundary.

From the variations of $C(H_i)$ and $D(H_i)$ in Fig. 8(b), it can be observed that the domain morphology evolves in a field dependent manner. In the low field regime, the onset of nucleation and rapid domain wall displacement significantly enhances boundary roughness and the effective wall length. This induces a sharp decline in compactness $C(H_i)$ alongside a marked increase in the fractal dimension $D(H_i)$. In the intermediate field range, the domain morphology evolves in a more continuous manner, consistent with predominantly smooth wall displacement. As the applied field approaches saturation, the domain walls are driven to straighten and eventually annihilate. This process minimizes the domain perimeter, resulting in the recovery of $C(H_i)$ and the reduction of $D(H_i)$. Overall, this evolutionary sequence is consistent with the standard domain wall picture for non-oriented silicon steel.

In addition to morphology descriptors, pixel-level segmentation metrics are reported to provide a direct measure of structural agreement with the ground truth. For each frame, we compute the numbers of true positives (TP), false positives (FP) and false negatives (FN) for each frame, and define:

$$\mathrm{IoU} = \frac{\mathrm{TP}}{\mathrm{TP} + \mathrm{FP} + \mathrm{FN}} \tag{12}$$

$$\mathrm{Dice} = \frac{2\mathrm{TP}}{2\mathrm{TP} + \mathrm{FP} + \mathrm{FN}} \tag{13}$$

Here TP denotes the number of pixels that are correctly predicted as belonging to the domain class, FP denotes the number of pixels that are predicted as domain but belong to the background in the ground truth, and FN denotes the number of pixels that are predicted as background but belong to the domain class in the ground truth. Table 3 summarizes the errors in $C(H_i)$ and $D(H_i)$ at representative field values, together with the mean IoU and Dice scores over the test sequences. Incorporating the boundary channel improves both pixel-level agreement and the fidelity of boundary related morphology descriptors, with the most pronounced benefit appearing in field ranges where domain-wall motion and wall roughening are dominant.

4.2. Ablation analysis of GLCM feature

In addition to binary magnetization maps and domain wall features, the gray-level texture in MOKE images encodes anisotropic statistical information that characterizes the evolution of domain patterns during the magnetization process. To quantify the contribution of these features, an ablation study was conducted in which the GLCM texture channels were excluded, while the network architecture and training protocol remained unchanged.

Fig. 9(a) illustrates the magnetic field dependence of three GLCM descriptors employed in the model, including contrast, homogeneity, and energy. The descriptors exhibit systematic variations with the applied field, indicating that gray-level statistical correlations evolve consistently with the magnetization process. Fig. 9(b) presents the direction-dependent responses in the form of polar plots. At 0 Oe, the angular distributions remain relatively dispersed, indicating weak magnetic anisotropy in the texture. As the applied field increases, the distributions progressively converge along a dominant direction, consistent with the field-induced alignment of the magnetic domain structure. Near saturation, a distinct directional orientation is observed, corresponding to a highly ordered magnetization state.

The quantitative improvement derived from incorporating GLCM texture channels is presented in Fig. 9(c). The full model achieves lower absolute prediction errors across the entire magnetic field range than the model without GLCM features, with a maximum relative improvement of 13.01% and an average improvement of 6.58%. These results indicate that the anisotropic gray-level statistical correlations provide information complementary to binary magnetization maps and domain wall features, thereby enhancing the robustness and accuracy of the magnetic domain evolution prediction.

Table 3
Effect of boundary features on domain-shape errors and pixel-level segmentation metrics.

Magnetic field (Oe)		Including boundary features	Without boundary features	Relative error (%)
C(H_i)	-500	0.087	0.075	13.79%
	-150	0.075	0.079	-5.33%
	150	0.064	0.061	4.69%
	500	0.128	0.107	16.40%
D(H_i)	-500	0.472	0.398	15.68%
	-150	0.701	0.748	-6.70%
	150	0.694	0.727	-4.76%
	500	0.487	0.427	12.32%
Mean IoU		0.89	0.81	
Mean Dice		0.93	0.88	

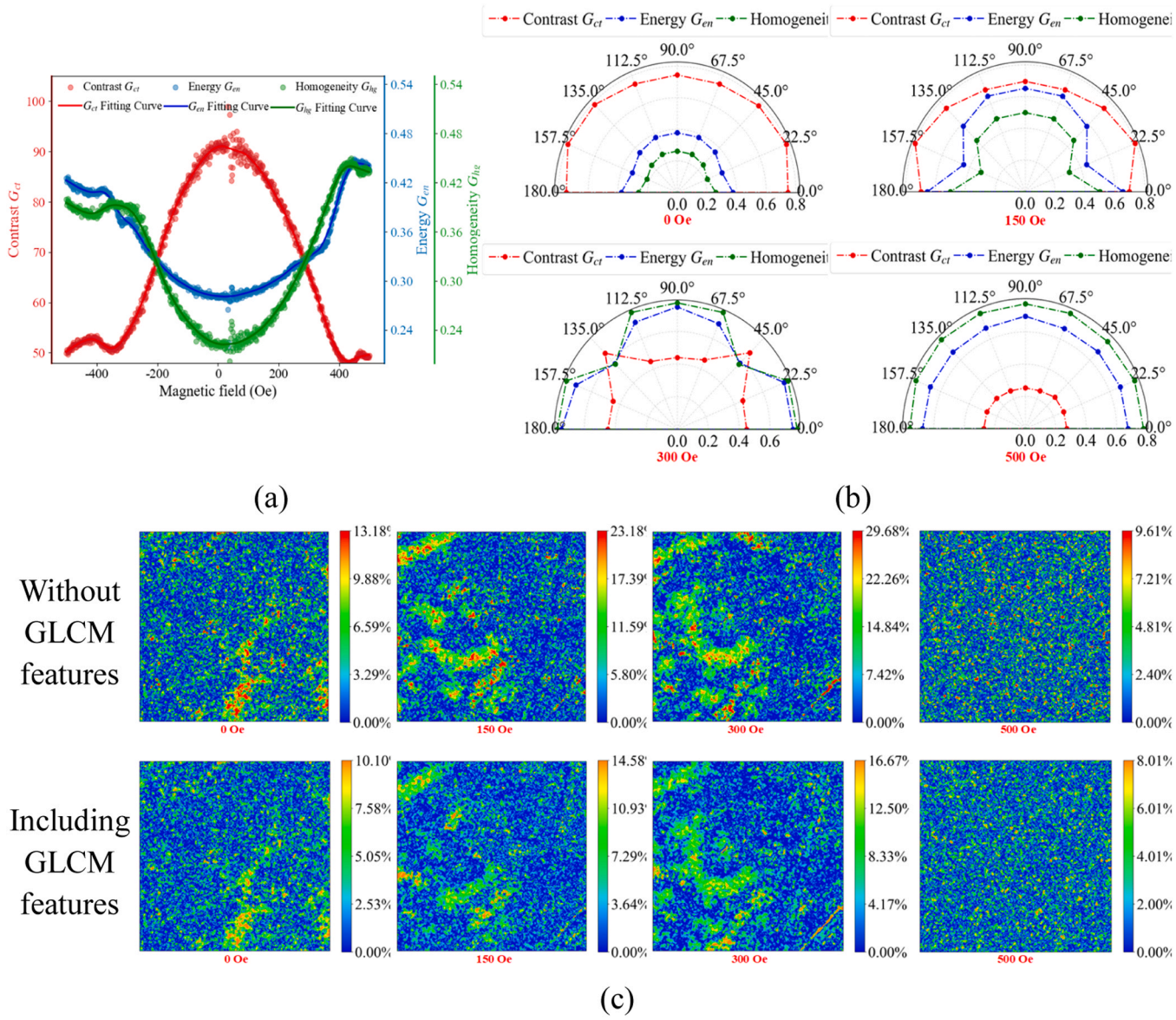


Fig. 9. (a) The changing trend of GLCM features with varying field strength, (b) The amplitude variation of GLCM features at different angles in magnetic domain images, (c) The absolute error of model predictions with and without GLCM features.

4.3. Comparison of prediction performance

In MOKE microscopy, the distinct contrast levels correspond to magnetic domains with opposite magnetization components along the sensitivity axis. Starting from a demagnetized state, the macroscopic magnetization evolution shows that some domains rotate to align with the applied field, while other opposing domains shrink in volume. To quantify the magnetization derived from the domain images, the normalized magnetization is defined as being proportional to the difference in area fraction between the two contrast regions:

$$m(H_i) = \frac{A_D(H_i) - A_B(H_i)}{A_D(H_i) + A_B(H_i)} \tag{14}$$

where A_D, and A_B denote the pixel areas of the dark and bright domains, respectively, and m represents the normalized magnetization at the applied field H_i.

As illustrated in Fig. 10(a), the domain morphologies exhibit significant spatial heterogeneity across different regions of the same specimen. Consequently, the magnetization trajectories calculated via Eq. (14) display distinct characteristics, as depicted in Fig. 10(b). To evaluate the model's generalization capability to unseen domain configurations, an independent test set was constructed using spatial regions excluded from the training dataset. The error distributions for four representative regions are presented in Fig. 10(c). Although the prediction error tends to correlate with morphological complexity, the average maximum absolute error remains below 9%, demonstrating robust magnetization estimation across heterogeneous domain patterns.

To quantitatively assess the predictive accuracy, the coefficient of determination (R^2) and the Root Mean Square Error (RMSE) are employed as evaluation metrics. For a dataset consisting of n samples, these metrics are defined as follows:

$$\mathrm{RMSE} = \sqrt{\frac{1}{n}\sum_{i=1}^{n}(y_i - \hat{y}_i)^2} \tag{15}$$

$$R^2 = 1 - \frac{\sum_{i=1}^{n}(y_i - \hat{y}_i)^2}{\sum_{i=1}^{n}(y_i - \bar{y})^2} \tag{16}$$

where y_i is the actual value, $\hat{y}_i$ is the predicted value, $\bar{y}$ is the average of

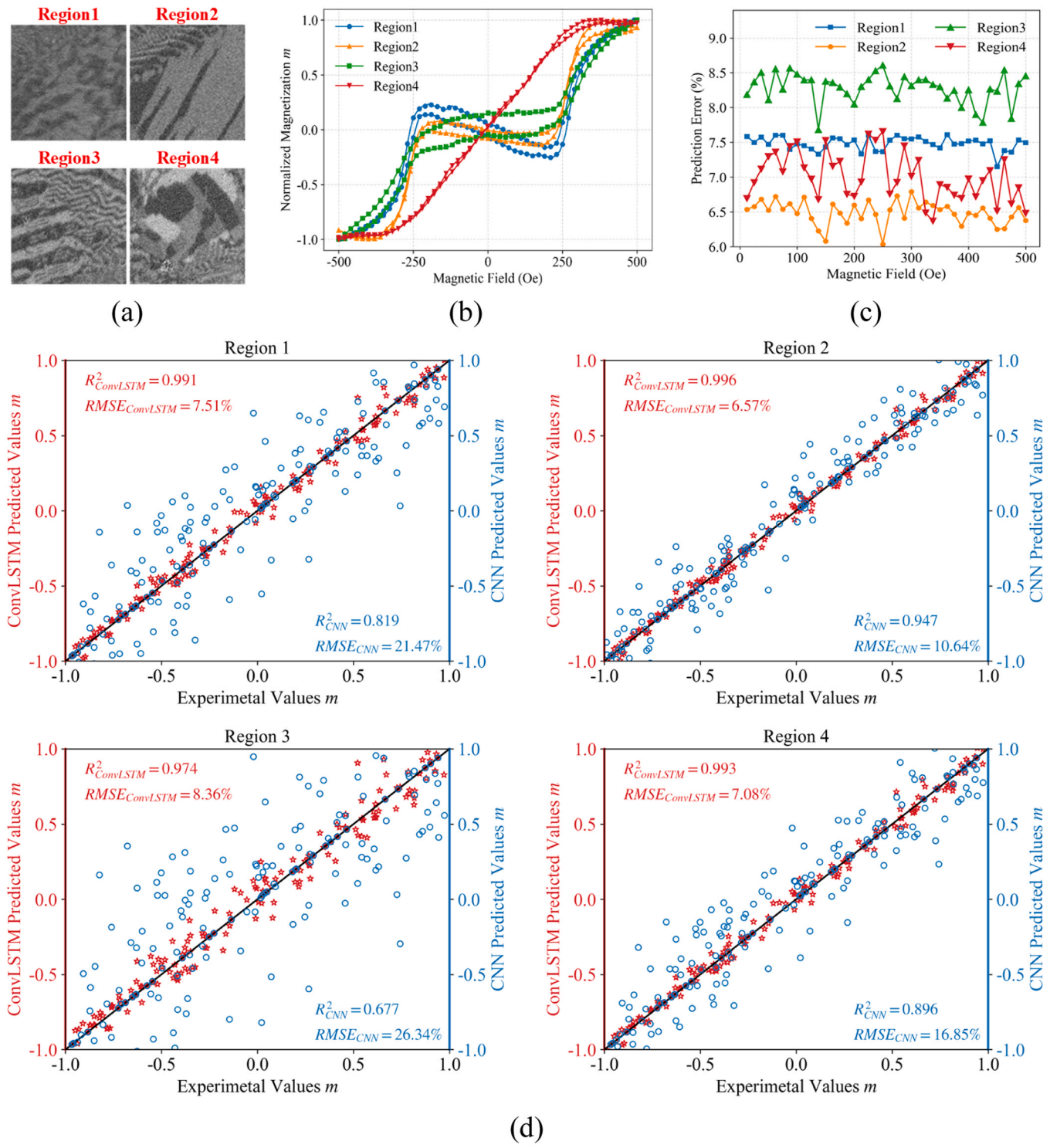


Fig. 10. Region dependent magnetization reconstruction and prediction. (a) representative domain patterns for four regions at the same applied field, (b) reconstructed normalized magnetization loops, (c) prediction errors across regions, and (d) predicted versus experimental magnetization for ConvLSTM and CNN on the same dataset.

the predicted values, and n is the total number of samples. In addition, the mean absolute error, abbreviated as MAE, is used in Table 4 to provide an intuitive measure of the average absolute deviation.

Complementing the qualitative assessment in Fig. 10(d), the proposed physics-guided ConvLSTM is quantitatively benchmarked against multiple baselines in Region 3 in Fig. 10(a), which exhibits the highest morphological complexity. The complete ConvLSTM model integrates domain wall boundary maps derived from the Sobel operator and texture descriptors computed via the GLCM as its physics-guided input channels. Two ablation variants were evaluated by excluding either the boundary or the texture channel while maintaining the backbone architecture unchanged. For comparison, a conventional CNN was trained to regress magnetization directly from individual frames without explicit temporal modeling, and a standard LSTM was implemented to capture temporal dependencies using globally pooled feature vectors. The quantitative results are presented in Table 4. The full ConvLSTM

Table 4
Quantitative comparison of model performance in Region 3.

Model	R^2	RMSE	MAE
Full ConvLSTM (include Sobel and GLCM)	0.974	8.36%	6.7%
ConvLSTM (without Sobel channel)	0.948	10.4%	8.2%
ConvLSTM (without GLCM channels)	0.928	11.7%	9.15%
CNN	0.677	26.34%	21.05%
LSTM	0.841	13.52%	10.5%

achieves superior overall performance, whereas the baselines and ablation variants demonstrate inferior accuracy. This outcome underscores the critical importance of synergizing temporal modeling with physics-guided feature extraction for predicting complex magnetic domain evolution.

Finally, the robustness of the model with respect to data partitioning was evaluated using five-fold cross validation. The values of the coefficient of determination R^2 and RMSE for each fold, along with their mean and standard deviation, are listed in Table 5. The low variance observed across the folds indicates that the magnetization prediction performance is statistically stable and insensitive to specific data splits.

Table 5
Results of 5-fold cross validation for the normalized magnetization $m(H)$.

Fold	R^2 for $m(H)$	RMSE for $m(H)$
1	0.954	0.072
2	0.951	0.075
3	0.957	0.069
4	0.949	0.077
5	0.953	0.073
Mean ± Std	0.953 ± 0.003	0.073 ± 0.003

5. Conclusion

This study proposes a ConvLSTM-based framework to predict the spatiotemporal evolution of magnetic domains in non-oriented electrical steel from time-resolved MOKE image sequences. By integrating convolutional feature extraction with recurrent temporal modeling, the proposed method effectively captures both spatial domain morphology and history-dependent dynamics, enabling the accurate prediction of domain wall motion and magnetization state transitions under time-varying magnetic fields.

Experimental results demonstrate that the integration of domain wall boundary features and gray-level texture descriptors yields significant improvements in predictive fidelity, particularly in regimes characterized by rapid domain wall motion and evolving texture anisotropy. Furthermore, the proposed preprocessing pipeline, incorporating the LaMa inpainting model, enhances dataset quality by effectively mitigating imaging artifacts while preserving the intrinsic intensity distributions. This establishes a more reliable foundation for both model training and performance evaluation.

In addition to domain pattern prediction, the proposed approach enables microstructural reconstruction and the prediction of magnetization evolution across spatially heterogeneous regions, demonstrating robust generalization on independent test sets. Consequently, this work establishes a practical data-driven framework for the analysis of magnetic microstructures and magnetization dynamics. It presents a novel methodological approach for the microstructural assessment and optimization of magnetic core materials under realistic excitation conditions. Future research will focus on extending the framework to other categories of magnetic materials and exploring the integration of advanced computer vision algorithms to further enhance prediction accuracy.

CRediT authorship contribution statement

Hao Zhang: Writing – review & editing, Writing – original draft, Methodology. **Qingxin Yang:** Supervision, Conceptualization. **Yifan Chen:** Supervision, Conceptualization. **Yongjian Li:** Supervision, Conceptualization. **Changgeng Zhang:** Supervision, Conceptualization.

Declaration of Competing Interest

The authors declare that they have no known competing financial interests or personal relationships that could have appeared to influence the work reported in this paper.

Acknowledgments

This work was supported in part by the National Natural Science Foundation of China, (No. 52277008, 52130710), the Hebei Provincial Natural Science Foundation Innovation Group Project (E2024202298), the CAS Superconducting Research Project (SCZX-0302), and the Central Government Guided Local Science and Technology Development Fund Projects (254Z2101G).

Data availability

Data will be made available on request.

References

[1] M. Gobbi, A. Sattar, R. Palazzetti, et al., Traction motors for electric vehicles: Maximization of mechanical efficiency – A review, Appl. Energy 357 (2024) 122496.
[2] J.M. Silveyra, E. Ferrara, D.L. Huber, et al., Soft magnetic materials for a sustainable and electrified world, Science 362 (6413) (2018) eaao0195.
[3] J. Muhlethaler, J. Biela, J.W. Kolar, et al., Improved Core-Loss Calculation for Magnetic Components Employed in Power Electronic Systems, IEEE Trans. Power Electron. 27 (2) (2012) 964–973.
[4] J. Reinert, A. Brockmeyer, R.W.A.A. De Doncker, Calculation of losses in ferro- and ferrimagnetic materials based on the modified Steinmetz equation, IEEE Trans. Ind. Appl. 37 (4) (2001) 1055–1061.
[5] G. Katsikas, C. Sarafidis, J. Kioseoglou, Machine Learning in Magnetic Materials, Phys. Status Solidi B 258 (8) (2021) 2000600.
[6] L. Exl, J. Fischbacher, A. Kovacs, et al., Magnetic microstructure machine learning analysis, J. Phys. Mater. 2 (1) (2018) 014001.
[7] M. Gusenbauer, H. Oezelt, J. Fischbacher, et al., Extracting local nucleation fields in permanent magnets using machine learning, Npj Comput. Mater. 6 (1) (2020) 1–10.
[8] H.Y. Kwon, H.G. Yoon, C. Lee, et al., Magnetic Hamiltonian parameter estimation using deep learning techniques, Sci. Adv. 6 (39) (2020) eabb0872.
[9] A. Agrawal, A. Choudhary, Perspective: Materials informatics and big data: Realization of the "fourth paradigm" of science in materials science, APL Mater. 4 (5) (2016).
[10] A. Talapatra, U. Gajera, P. P S, et al., Understanding the Magnetic Microstructure through Experiments and Machine Learning Algorithms, ACS Appl. Mater. Interfaces 14 (44) (2022) 50318–50330.
[11] Alhada–Lahbabi K., Deleruyelle D., Gautier B. Reinforcement Learning-Assisted Ferroelectric Domain Wall Design Using a Machine Learning Phase-Field Surrogate.
[12] J.F. Kong, Y. Ren, M.S.N. Tey, et al., Quantifying the magnetic interactions governing chiral spin textures using deep neural networks[A], arXiv (2023).
[13] D.B. Lee, H.G. Yoon, S.M. Park, et al., Estimating the effective fields of spin configurations using a deep learning technique, Sci. Rep. 11 (1) (2021) 1–11.
[14] N. Mehmood, J. Wang, Q. Liu, Machine learning estimation of magnetic parameters and classification of magnetic vortex states, J. Appl. Phys. 132 (4) (2022).
[15] H.Y. Kwon, H.G. Yoon, S.M. Park, et al., Magnetic State Generation using Hamiltonian Guided Variational Autoencoder with Spin Structure Stabilization, Adv. Sci. 8 (11) (2021) 2004795.
[16] M. Kawaguchi, K. Tanabe, K. Yamada, et al., Determination of the Dzyaloshinskii-Moriya interaction using pattern recognition and machine learning, Npj Comput. Mater. 7 (1) (2021) 1–7.
[17] D. Wang, S. Wei, A. Yuan, et al., Machine Learning Magnetic Parameters from Spin Configurations, Adv. Sci. 7 (16) (2020) 2000566.
[18] A. Dehghani, H.M.Z.H. Moazam, F. Mortazavizadeh, et al., Comparative evaluation of LSTM, CNN, and ConvLSTM for hourly short-term streamflow forecasting using deep learning approaches, Ecol. Inform. 75 (2023) 102119.
[19] Y. Xu, J. Hou, X. Zhu, et al., Hyperspectral Image Super-Resolution With ConvLSTM Skip-Connections, IEEE Trans. Geosci. Remote. Sens. 62 (2024) 1–16.

[20] X. Shi, Z. Chen, H. Wang, et al., Convolutional LSTM Netw. A Mach. Learn. Approach Precip. Nowcasting[A] (2015) (arXiv,).
[21] A. Hubert, R. Schäfer, Magnetic Domains: The Analysis of Magnetic. Microstructures, Springer, 1998.
[22] I.V. Soldatov, R. Schäfer, Advances in quantitative Kerr microscopy, Phys. Rev. B 95 (2017) 014426.
[23] M. Jovičević-Klug, P. Jovičević-Klug, J. McCord, et al., Investigation of microstructural attributes of steel surfaces through magneto-optical Kerr effect, J. Mater. Res. Technol. 11 (2021) 1245–1259.
[24] I.V. Soldatov, J. Zehner, K. Leistner, et al., Advanced, Kerr-microscopy-based MOKE magnetometry for the anisotropy characterisation of magnetic films, J. Magn. Magn. Mater. 529 (2021) 167889.
[25] S. Kuno, S. Deguchi, S. Sumi, et al., Estimation of TbCo composition from local-minimum-energy magnetic images taken by magneto-optical Kerr effect microscope by using machine learning, APL Mach. Learn. 1 (4) (2023) 046111.
[26] Suvorov R., Logacheva E., Mashikhin A., et al. Resolution-robust Large Mask Inpainting with Fourier Convolutions[A]. arXiv, 2021.
[27] J. Jam, C. Kendrick, K. Walker, et al., A comprehensive review of past and present image inpainting methods, Comput. Vis. Image Underst. 203 (2021) 103147.
[28] N. Otsu, A threshold selection method from gray-level histograms, Automatica 11 (285-296) (1975) 23–27.
[29] M.P. Ekstrom, Digital image processing techniques[M], Academic Press, 2012.
[30] P. Gao, Y. Song, M. Song, et al., Extract nanoporous gold ligaments from SEM images by combining fully convolutional network and Sobel operator edge detection algorithm, Scr. Mater. 213 (2022) 114627.
[31] R.M. Haralick, K. Shanmugam, I.H. Dinstein, Textural features for image classification, IEEE Trans. Syst. Man. Cybern. (6) (2007) 610–621.
[32] K. Funahashi, Y. Nakamura, Approximation of dynamical systems by continuous-time recurrent neural networks, Neural Netw. 6 (6) (1993) 801–806.
[33] B.-S. Han, D. Li, D.-J. Zheng, Y. Zhou, Fractal study of magnetic domain patterns, Phys. Rev. B 66 (2002) 014433.